A model for the microstructure behaviour and strength evolution in lath martensite

E.I. Galindo-Nava, P.E.J. Rivera-Díaz-del-Castillo

Department of Materials Science and Metallurgy, University of Cambridge, UK

Abstract

A new model describing the microstructure and strength of lath martensite is introduced. The packet and block size were found to linearly depend on the prior–austenite grain size when introducing relevant crystallographic and geometric relationships of their hierarchical arrangements. A mechanism for the lath boundary arrangement within a block is postulated to ensure complete carbon redistribution to the lath boundaries. Accordingly, the dislocation density is obtained by considering the lattice distortion energy within a lath being equal to the strain energy of the dislocation density at the lath boundaries. Tempering effects are introduced by estimating the extent of carbon diffusing away from the lath boundaries; this mechanism relaxes the Cottrell atmospheres of lath dislocations and coarsens the boundaries. The yield stress and microstructure evolution during tempering is successfully predicted by combining these results. The model is further extended to describe the yield stress in dual–phase steel microstructures by employing the iso–work principle. The model predictions are validated against experimental data in seven martensitic and five dual–phase steels, where the prior–austenite grain size, carbon content, tempering conditions and martensite volume fraction are employed as input. These results cover wide composition, initial microstructure and tempering conditions.

Keywords: Martensite; Yield Strength; Dislocations; Cottrell atmospheres; Steels

1. Introduction

Lath martensite is one of the most important phases in low and medium carbon steels for high–strength applications. During quenching, the transformation from austenite to martensite produces high shear strains from the supersaturated carbon content in the

matrix and thin laths form in order to minimise the strain energy [1, 2]. This process is characterised by inducing a high dislocation density, being this one of the main contributors to the high strength of martensite [3, 4]. The transformation process also results in a complex microstructure, consisting of hierarchically arranged substructures within the prior–austenite grains, namely packets and blocks of individual laths.

Extensive experimental characterisation has been performed to aid unravelling the complex nature of lath martensite. For instance, several authors have employed electron–backscattering diffraction measurements to identify the microstructural and crystallographic features of martensite [2, 5–8]. They have concluded that the hierarchical arrangement of packets/blocks and lath boundaries allows to accommodate the crystallographic shears of the transformation; this ensures that the net strain in the prior austenite grain is pure dilatation. Additionally, experimental evidence has shown that the prior–austenite grain size has a strong effect on the scale of packets and blocks and almost negligible effects on the lath substructure development [9–12]. This implies that the microstructure in the lath boundaries is practically independent of the prior–austenite grain size.

Atom–probe tomography has shown that carbon atoms tend to segregate towards the lath boundaries [13]. It has been suggested in low–carbon steels that Cottrell atmospheres form at the lath boundaries for as–quenched conditions [14, 15]; further carbon redistribution occurs during tempering forming precipitates at the boundaries [13]. Chang *et al.* [16] observed in two steels containing 0.45 and 0.85 at% carbon that the matrix was almost depleted in carbon, whilst carbon–rich regions extending for radial distances of at least 3 nm could be seen from the dislocation lines [17]. Wilde *et al.* [14] extended this work to quantify the carbon atom distribution and concentration within the atmospheres; they found the carbon saturation in the atmosphere to be at about 7–8 at%. Sherman *et al.* [18] have attributed in a medium carbon steel (1.31 at% carbon) the formation of Cottrell atmospheres in the vicinity of the dislocation cores in the martensite matrix, and that approximately 90% of carbon atoms are located within the range of the atmospheres. The remaining carbon was located in thin films of retained austenite. Interestingly, the

lath boundaries show a carbon peak concentration of ~ 7 at% in the specimen with the highest cooling rate in as–quenched conditions; this value corresponds to the concentration saturation of a Cottrell atmosphere. TEM measurements showed no clear images or diffraction patterns of either austenite or carbides at the lath boundaries for this case. Similarly, Miller *et al.* [13] measured in Fe–Ni–C lath martensite for as–quenched conditions a peak concentration at the lath boundaries of 7.8 at%. One aim of this work is to employ these results to propose a model being able to describe the structure of lath martensite, and to relate it to its mechanical properties in as–quenched and tempered conditions.

There are a number of strengthening mechanisms in the martensitic structure, including high–angle grain boundary strengthening [9], increase in the dislocation density [2], and carbide precipitation during tempering [4]. Although the occurrence of these mechanisms is well accepted, there are limited microstructure–sensitive models linking the evolution of the martensitic structure and its respective strength for as–quenched and tempered conditions; this can be due to the fact that models for describing the dislocation density as a function of carbon content and processing parameters are practically non–existent. This is also reflected by the fact that existing modelling approaches for martensite strengthening and dual–phase steels require the "calibration" of the dislocation density to reproduce the experiments [19–21]. This in turn leads to inaccurate estimations on the individual effects of the respective strengthening mechanisms, and becomes more prominent when tempering effects are also introduced. For instance, some authors have considered in the yield strength equation a stress term of carbon acting as interstitial solid solution, as if the microstructure were ferritic [15, 22]. However, as carbon strongly segregates to the lath boundaries and most likely forms Cottrell atmospheres, this suggests that the carbon content is mostly related to the dislocation density increment rather than solid solution strengthening [23].

The objective of this work is to introduce a model for describing the microstructure and strength evolution of lath martensite and to validate it with low and medium carbon martensitic and dual–phase steels. This includes postulating: 1) crystallography–

based relationships interlinking the prior–austenite grain, packet and block boundaries; 2) physics–based expressions linking carbon content with the dislocation density and lath boundary width; 3) predicting the yield strength evolution of martensitic and dual–phase steels as a function of the internal microstructure and carbon content; and 4) describing carbon diffusion effects during tempering and the respective recovery effects. Possible scenarios for alloy and heat treatment design to increase the yield strength are also explored. It is demonstrated that the complex martensitic hierarchical structure can be described by the present model by employing as input parameters the prior–austenite grain size, carbon content and tempering conditions. A summary of the main equations for the strength and microstructure in martensite is shown in the Appendix.

2. Materials and processing conditions

Table 1 shows the chemical composition and denomination of the materials studied in this work; all experimental results have been obtained from the literature. They cover seven martensitic and five dual–phase steel families. In most cases, low alloying additions of up to six substitutional elements are present. Contributions from other elements are neglected.

Table 2 shows the initial microstructure and tempering conditions for all steels considered here. t and T stand for the tempering time and temperature, respectively; D_g stands for the prior–austenite grain size; r_p and f_p are respectively the mean radius and volume fraction of the carbides forming during tempering; and V_f is the martensite volume fraction of the dual–phase steels. It is worth noting that for Mart1 and Mart5, no precipitation characterisation is shown since only the microstructure is described and no yield strength is predicted. Additionally, no prior–austenite grain size and carbide characterisation were reported for Mart6, and these values were assumed to be consistent with typical tempering conditions [4]. In the case of DP1, DP2 and DP3, no carbide characterisation was reported, and fixed volume fraction and particle size were assumed in all cases to be consistent with the experimental characterisation in pure martensitic steels, as it has been shown that tempering in dual–phase steels display similar precipitation kinetics

than pure martensitic steels [24].

3. Microstructure evolution modelling

This section presents the theoretical aspects of the model to describe the packet/block and lath size, as well as the dislocation density as a function of the prior–austenite grain size, carbon content and tempering conditions. This work is defined upon four main assumptions to simplify the analysis:

i) It is assumed that martensite has been fully formed at room temperature after quenching. No cooling rate and M_s effects are considered to affect the initial microstructure.

ii) No precipitation kinetics during tempering is described and the volume fraction and mean carbide radius are obtained directly from the experiments.

iii) Only carbon is assumed to control martensite's behaviour and to fully segregate to the lath boundaries. No other compositional effects in the martensitic structure evolution are considered.

iv) A simplified martensite morphology is considered: prismatic prior–austenite grains with hexagonal shape, packets of polygonal shape, and rectangular blocks and laths. Their depth equals to the prior–austenite grain size.

Assumption *i*) is consistent with the fact that the phase transformation occurs at a very high speed and the quenching rates for the conditions tested in this work are very high [15, 25]; additionally, Villa *et al.* [26] have found no effect of the cooling rate on the microstructure arrangement in a number of steels. However, other phases can be present such as thin films of retained austenite at the lath boundaries when increasing carbon content [27–29] or carbides at lath boundaries or their interiors. Retained austenite can affect the yield stress by removing carbon atoms from the matrix and softening the steel, since carbon is more soluble in austenite [1]. Additionally, Morito *et al.* [29] have suggested that retained austenite films can also increase the work–hardening rate in martensite by

increasing the number of barriers for dislocation motion. The presence of carbides can aid in increasing the yield stress in the steel by precipitation of non–shearable particles [30], although they also remove carbon atoms from the laths and potentially soften the matrix. The interplay between precipitation hardening and matrix softening depends on the processing conditions and requires an accurate description of precipitation evolution [4]. Nevertheless, assumption *ii*) is introduced to account for precipitation during tempering and its effect in the yield stress. The effective carbon content in the matrix for the dislocation density is considered by removing the carbon content in the precipitate from the total content in the steel.

Assumption *iii*) is introduced since most of the steels tested in this work contain low alloying additions of several substitutional elements (Table 1). In the case of Mart1, a highly alloyed steel, only the packet size is predicted in this work. Additionally, although carbon atoms can also be located at dislocations in the lath interiors, a very high segregation fraction at the lath boundaries has been found with atom–probe tomography [14,15].

Assumption *iv*) is introduced based on experimental observations of a typical martensite structure with a three–level hierarchy and its complex morphology [4, 5]; since microstructure characterisation has been estimated from two dimensional micrographs, the volume of these structures is better represented by cross–sectional areas of constant depth (D_g). Additionally, since packets display irregular shapes [31] and only the mean sizes (d_{packet}) are usually reported, polygons with cross–sectional area equal to the area of cubic packets with d^2_{packet} are considered for simplicity and to be consistent with experimental observations. Figure 1(a) shows a schematic representation of the martensite lath, block, and packet distributions in a prior–austenite grain size. The solid thin lines represent the packet boundaries, the dashed and dotted lines represent block and lath boundaries, respectively. The packet volume is also shown in the Figure and the volume of a block is $d_{block}d_{packet}D_g$, where d_{packet} and d_{block} are the packet and block size, respectively. Figures 1(a),(c) and (e) show a schematic representation of the hierarchical nature of the martensitic structure produced by carbon redistribution; the dotted line in (e) represents a boundary–dislocation.

3.1 Martensite grain boundaries: hierarchical effects

During martensite formation, an austenite grain is divided into packets (laths with a common transformation habit plane), which are further subdivided into blocks (laths with the same orientation variants). This implies that the prior–austenite volume $V_{PAGS} = \frac{3\sqrt{3}}{8} D_g^3$ is composed by the total packet volume $N_p V_{packet}$, where N_p is the total number of packets per austenite grain and V_{packet} is the mean packet volume; accordingly, the volume of a packet is composed by the total block volume $N_p V_{block}$, where N_p is the total number of blocks per packet and V_{block} is the mean block volume. By taking assumption iv) into consideration, the cross–sectional area of a packet and block are d_{packet}^2 and $d_{block} d_{packet}$, respectively; the previous relationships are mathematically expressed as:

$$\begin{aligned} V_{PAGS} &= N_p V_{packet} = N_p d_{packet}^2 D_g \\ V_{packet} &= N_b V_{block} = N_b d_{block} d_{packet} D_g. \end{aligned} \tag{1}$$

It is worth noting that the prior–austenite volume is taken to be equal to the martensite volume, *i.e.* no dilatation is introduced, since measurements of D_g are performed directly on the martensite, where dilatation has already occurred. N_p and N_b can be known from the crystallographic arrangements of the transformation.

Several authors have confirmed that the number of packets per austenite grain is dictated by the number of variants in the Kurdjumov–Sachs (K–S) orientation relationship for low and medium carbon martensite [2, 5–7, 9, 32]:

$$\{111\}_\gamma || \{011\}_{\alpha'} \quad \langle 110 \rangle_\gamma || \langle 111 \rangle_{\alpha'}.$$

Since packets are formed by laths sharing a common habit plane, there are four possible variants of the $\{111\}_\gamma$ planes in the K–S relation, giving the total packet number per austenite grain equal to $N_p = 4$; this value is consistent with experimental observations [2, 32]. On the other hand, the strain controlling the martensitic transformation is composed by a dilatation, remaining constant for each K–S relation, and a shear strain differing from each variant [32]. Hence, all six lath orientation variants in a given packet should be present in order to minimise the elastic energy and decrease the overall strain [5, 7, 32].

This indicates that the possible number of blocks per packet should be $N_b = 6$. Morito *et al.* [31] have outlined that in a packet there are 3 blocks and each block contains 2 sub–blocks where laths of two specific K–S variant groups are present; sub–blocks in a block have low misorientation angles. Since sub–blocks and blocks both define the lath boundary distribution domain [32], no distinction is made between them at this stage, giving a total number of 6 structures of laths with common orientation. Combining these results, the packet and block size are equal to:

$$\begin{aligned} d_{packet} &= \sqrt{\frac{3\sqrt{3}}{8N_p}}D_g = \sqrt{\frac{3\sqrt{3}}{32}}D_g = 0.40D_g, \\ d_{block} &= \frac{1}{N_b}d_{packet} = \frac{1}{6}d_{packet} = 0.067D_g. \end{aligned} \tag{2}$$

Figure 2 shows the relationship between D_g and (a) packet and (b) block size for a number of steels with different carbon content, Mar4, Mar5 and two steels with 0.2C wt% obtained from [9]. The solid lines represent the predictions employing equations 2 and the bullet points represent the experiments.

The model displays remarkable agreement with the measurements, indicating that the packet and block size are composition–independent, although constant block sizes are apparent for $D_g > 75$ μm; this can be due to the formation of additional sub–blocks [9]. The model predictions may differ for $D_g < 10$ μm, since Morito *et al.* [33] have shown that the linear relationship breaks down and not all blocks can form when the prior–austenite grain size is lower than 5–10 μm. This will affect the number of packets per prior–austenite and blocks per packet, since not all the crystallographic variants of K–S relation are present [33]. This can be explored more in detail in future work. This result also allows us to fully describe the number density of high–angle grain boundaries if the prior–austenite grain size is known and the complexity of the martensitic structure can be further simplified. Our study will now focus on describing the microstructure of the martensite laths, since they are closely related to the dislocation density and the material's strength [34].

At the sub–block level, extensive experimental and theoretical evidence has shown

that lath boundary formation is determined by the lattice deformation, which dictates the variant selection of a lath, whilst holding the same crystallographic orientation within a block [32, 35, 36]. Whilst this result provides qualitative insights into the nature of lath boundary formation, there is less evidence on how to link the lath size with the lattice strain or carbon content, since the lath size is independent of the prior–austenite grain size [9]. Based on the fact that laths form to minimise the strain energy produced by the lattice distortions around carbon atoms, a simple mechanism is proposed to determine the lath size: Since no significant residual strains are present in the martensitic microstructure [32], complete carbon redistribution to the lath boundaries should occur within a block (assumption *iii*)); additionally, the lattice strain at this length scale is accommodated by the formation of interfacial dislocations at the lath boundaries [34]. This phenomenon suggests that Cottrell atmospheres form within the boundaries, and the randomly distributed carbon atoms in the austenite phase (lath interiors) should relocate around these atmospheres [15]. Figures 1(b) and (c) show a schematic representation of a cross–section in the block interiors showing carbon redistribution from the austenite (b) to the lath boundaries in (c); the latter scheme is supported by atom–probe experiments [15]*. This implies that the lath boundary spacing (lath size) is such that it ensures complete carbon segregation within a block and the extent of carbon segregation in a lath boundary is controlled by the thickness of a Cottrell atmosphere $d_{Cottrell}$. Thus, the lath size after quenching ($d_{lath,0}$) is proportional to the Cottrell atmosphere and the effective carbon content available for segregation from the austenite. If a cross–sectional area of a lath is considered, this is mathematically expressed as:

$$d_{lath,0} = d_{Cottrell}\frac{l_C^2}{b^2}, \tag{3}$$

where $l_C = b/(x_C^{\alpha'})^{1/3}$ is the mean carbon spacing [37], b is the magnitude of the Burgers vector and $x_C^{\alpha'}$ is the carbon atom fraction in the martensitic structure; l_C^2/b^2 represents the effective carbon content available for segregation. $x_C^{\alpha'}$ is obtained by removing the carbon content in the precipitate (based on the experimental particle fraction f_p) from

*It is assumed that a Cottrell atmosphere is defined as the radial distance between the dislocation core and a critical distance where its hydrostatic interaction with carbon is practically null [14].

the total concentration. If cementite is considered this gives: $x_C^{\alpha'} = x_C(1 - f_p/4)$, where x_C is the total carbon content in the steel (obtained from Table 1). It is worth noting that the previous equation may not be valid for higher carbon content, since the presence of lath–boundary carbides and retained austenite films can reduce the frequency of Cottrell atmospheres and carbon content [38]. The thickness of a Cottrell atmosphere has been experimentally found to be approximately 7 nm [14]. Figure 2(c) shows the model predictions for the lath size (width) for various carbon concentrations and the comparison against experimental measurements for as–quenched conditions (no precipitates are present) in Mar2, Mart7[†], and two steels with composition 0.2C–0.01Ni–0.02Cr (wt%) and other minor substitutional additions and 0.098C–0.25Si–0.5Mn–0.87Cu–0.31Ni–9Cr–0.39Mo–1.87W–0.05Nb (wt%); the experimental data were obtained from [39,40] and [41], respectively. The Burgers vector was considered equal to $b = 0.286$ nm. The model shows good agreement with the experimental trends as the lath size is finer as the carbon content increases. Additional results on lath size predictions are shown in Section 3.2 (via the dislocation density) and in the Results section for Mar4 and Mart7, where tempering effects have also been included. Once the complete boundary arrangement has been described, the dislocation density at the lath boundary level can be obtained.

3.2 Dislocation density

During quenching, carbon atoms redistribute into lath boundaries. Since no cooling rate and M_s effects are initially considered, it is assumed that carbon atoms segregate into lath boundaries in the form of Cottrell atmospheres around interfacial dislocations [14,15]. This assumption is consistent with Olson and Cohen's classical martensite formation theory [34], as they propose that a number of interfacial dislocations must nucleate and form lath boundaries in order to conceal the local distortions produced by the carbon atoms. However, carbon segregation at the lath boundaries can also be due to the presence of other phases such as thin films of retained austenite or carbides, although this mechanism depends on prior processing conditions. For instance, Sherman *et al.* [18] have stud-

[†]These data show the measurements at the lowest tempering temperature which show negligible coarsening effects [25].

ied carbon redistribution in a medium–carbon steel with different fractions of retained austenite. In the samples with the lowest austenite volume fraction (highest cooling rate) for as–quenched conditions, the carbon concentration at the lath boundaries corresponds to the concentration saturation of a Cottrell atmosphere ($\sim$ 7 at%). Additionally, their TEM measurements showed no clear images or diffraction patterns of either austenite or carbides at the lath boundaries. This result supports the assumption that carbon redistribution can be due to Cottrell atmospheres for the case when the fraction of retained austenite and carbides is very low.

Carbon redistribution around interfacial dislocations suggests considering the dislocation and lattice strain energy at the lath boundaries to be equal, in order to ensure that the overall strain during the transformation is pure dilatation [32]. If the lath boundaries are formed by dislocation loops [34], the energy per unit volume required to nucleate an interfacial dislocation of length $4d_{lath,0}$ (lath boundary perimeter) is given by [30] $E_{disl} = \frac{1}{2}\mu b\rho(4d_{lath,0})/4$, where ρ is the lath dislocation density, $\mu = 80$ GPa is the shear modulus and the $\frac{1}{4}$ factor accounts for the shared dislocation density on adjacent lath boundaries. On the other hand, the lattice strain energy produced during the phase transformation can be estimated by the Stibitz equation on the lath boundaries [42]. Carbon redistribution requires introducing an additional factor to account for the localised distortions at the lath boundaries. This is given by comparing the cross–sectional area where carbon locates in the lath boundaries (around a dislocation), $A_{lath} = \left((d_{lath,0} + d_{Cottrell})^2 - (d_{lath,0} - d_{Cottrell})^2\right) = 4d_{lath,0}d_{Cottrell}$, and the equivalent area when carbon is randomly distributed in the austenite, $A_{random} = d_{lath,0}^2$. Figures 1(d) and (e) show a schematic representation of the comparison between these areas; the dotted line represents a boundary–dislocation. The lattice strain energy can be expressed as [42]:

$$E_{lattice} = \frac{3E\varepsilon^2}{2(1+2\nu^2)}\frac{A_{lath}}{A_{random}} = \frac{3E\varepsilon^2}{2(1+2\nu^2)}\frac{4d_{Cottrell}}{d_{lath,0}}, \tag{4}$$

where $E = 211$ GPa is the Young's modulus, $\nu = 0.3$ is the Poisson ratio, and ε is the lattice strain produced by carbon redistribution. Equating E_{disl} and $E_{lattice}$, the dislocation density becomes:

$$\rho = \frac{3E}{(1+2\nu^2)\mu}\frac{4\varepsilon^2 d_{Cottrell}}{d_{lath,0}^2 b}. \tag{5}$$

It is interesting noting that this equation is very similar to that employed by a number of authors to estimate the dislocation density in lath martensite by neutron diffraction measurements [3, 25]; however, equation 5 successfully illustrates the link between lath size and carbon content. ε can be calculated by obtaining the root mean square of the lattice strain induced on each lattice direction from FCC to the martensitic structure: $\varepsilon = \sqrt{\varepsilon_x^2 + \varepsilon_y^2 + \varepsilon_z^2}$; this can be done since all crystallographic distortions have been concealed by packet and block formation. Experimental evidence has shown that martensite with carbon concentration below 0.6 wt% shows almost no tetragonality since the lattice parameter aspect ratio $c_{\alpha'}/a_{\alpha'}$ is very low [35]. For instance, Xiao *et al.* [43] have measured the lattice parameter in martensite to be practically constant in steels with carbon content up to ∼0.6 wt%, where the maximum $c_{\alpha'}/a_{\alpha'}$ ratio is 1.006. In addition, Udyansky *et al.* [44] have predicted that martensite with carbon content less than 0.14–0.16 wt% has a BCC structure at room temperature. Nevertheless, Morito *et al.* [5] have shown in ultra–low carbon steels (carbon content equal to 0.0049 wt%) that lath martensite still forms even for such low carbon content. This suggests that the non–symmetrical distortions produced by carbon atoms occur locally in the lath boundaries, increasing the dislocation density during the transformation from austenite to martensite [1]. Considering the cell parameters of martensite $a_{\alpha'} = 0.288$ nm [43] and austenite $\frac{\sqrt{2}}{2}a_\gamma = \frac{\sqrt{2}}{2}0.355$ nm [4], where the $\frac{\sqrt{2}}{2}$ factor accounts for the rotation term of the Bain transformation in a unit cell [1, 36], the lattice strain on each direction equals: $\varepsilon_x = \varepsilon_y = \varepsilon_z = \frac{\frac{\sqrt{2}}{2}a_\gamma - a_{\alpha'}}{\frac{\sqrt{2}}{2}a_\gamma}$.

Figure 2(d) shows a comparison between the predicted dislocation density for different carbon contents (in wt%) and experimental estimations employing transmision–electron microscopy and the mean intercept method for as–quenched conditions; the experimental data were obtained from [2]. The model displays good agreement with experimental trends although considerable scatter in the measurements is observed for higher carbon concentrations; this can be due to the formation of plate martensite containing twins and reducing the dislocation density. Additional predictions for ρ are shown in the Results

section. These results show that the dislocation density and the lath thickness can be estimated if the carbon content is known.

3.3 Martensite tempering

Two major microstructural changes occur during tempering affecting the material's strength [4]: 1) Carbon diffusion coarsens the lath boundaries [45]; dislocation recovery also occurs since the lattice strains are released by carbon migration [41]. 2) Fine carbide precipitation occurs as a result of carbon migration. Boundary coarsening can be estimated by following Cottrell and Bilby's original approximation on carbon segregation towards dislocations [46]: The lath thickness increases by the decrease in the population of Cottrell atmospheres when carbon atoms diffuse away from the dislocations:

$$d_{lath} = d_{lath,0} + \lambda_0 x_C^{\alpha'} \sqrt{D_{diff} t}, \tag{6}$$

where $d_{lath,0}$ is the lath thickness after quenching, $\sqrt{D_{diff}t}$ is the mean carbon diffusion length, $D_{diff} = 6.2\times10^{-7} \exp\left(-\frac{80{,}000}{RT}\right)$ m^2/s is the diffusion constant of carbon in iron [1], $R = 8.31$ J K^{-1}mol^{-1} is the gas constant and $\lambda_0 = b/d_{Cottrell}$ is a constant accounting for a diffusion barrier for carbon atoms segregated into the Cottrell atmospheres.

Carbide precipitation may increase the matrix yield strength by the dispersion of non–deformable particles impeding dislocation glide [47]. Such effect is prescribed by the Orowan–Ashby mechanism, where the additional applied stress for dislocations to bypass fine carbides is [25, 48]:

$$\sigma_p = 0.26 \frac{\mu b}{r_p} f_p^{1/2} \ln\left(\frac{r_p}{b}\right), \tag{7}$$

where f_p and r_p are the volume fraction and mean radius of the carbides, respectively (Table 2). Yield strength in a martensitic steel can now be obtained, as the high–angle grain boundaries and dislocation density have been characterised.

4. Yield stress

Four strengthening contributions are considered: 1) Solid solution; 2) grain boundary (Hall–Petch); 3) dislocation accumulation; and 4) precipitation hardening. Item 1) ac-

counts for substitutional solution strengthening, since all the studied steels in this work contain various alloying elements. The Fleischer equation [23,49] is employed to estimate solid solution strengthening. It is worth noting that since carbon atoms are trapped at the lath boundaries (via the dislocation network), no interstitial solid solution is needed in the strengthening equation. For item 2) Morito *et al.* [9] have pointed out that the block size can be considered as the "effective" grain size; similar conclusions have been outlined by other authors [50,51]. Moreover, it has been shown that the prior–austenite grain, packet and block boundaries are all interconnected, hence it is consistent to consider the block boundaries as the effective barriers for dislocation motion. The strengthening contribution by the dislocation density is given by the Taylor equation [52]. The effective martensite strength σ_{Mart} is given by the combination of items 2) and 3). Item 4) is given by equation 7. When more than one strengthening mechanism is present (martensite+precipitation hardening), a mixture rule is introduced to account for their combined effects [25,53]. The yield strength can therefore be calculated from:

$$\begin{aligned} \sigma_{Mart} &= \frac{300}{\sqrt{d_{block}}} + 0.25 M \mu b \sqrt{\rho}, \\ \sigma_Y &= \sigma_0 + \sum_i (\beta_i^2 x_i)^{1/2} + \left(\sigma_{Mart}^2 + \sigma_p^2\right)^{1/2}, \end{aligned} \tag{8}$$

where $\sigma_0 = 50$ MPa is the lattice friction stress [22], x_i is the atom fraction of substitutional element i and β_i is the strengthening constant related to the lattice and modulus mistift of element i with respect to iron; the Hall–Petch constant (300 MPa μm$^{1/2}$) was adjusted to predict the yield stress in the steels tested and this value is consistent with other experimental results [9,10]; and M is the Taylor orientation factor. Details on β_i estimation are shown in the Appendix.

4.1 Dual–phase steels

Dual–phase steels are typically low-carbon steels with a composite microstructure containing hard martensite and soft ferrite. These alloys possess good tensile strength and ductility, the former being imparted by martensite, whereas the latter is mostly controlled by the volume fraction of ferrite. The ferrite grains plastically deform earlier than

the martensite grains to accommodate strain; as the stress increases, strain localisation occurs at the ferrite/martensite boundaries produced by geometrically–necessary dislocations [54]; this mechanism prevents describing the yield strength as a simple mixture rule, since strain partitioning is heterogeneous [55]. However, the partitioning behaviour in these steels is still not fully understood [56]. Bouaziz and Buessler [57] have proposed an alternative approach to describe plasticity in multiphase materials based on the assumption that the mechanical work on each constituent is equal: $\sigma_1\varepsilon_1 = \sigma_2\varepsilon_2$, where $\sigma_{1,2}$ and $\varepsilon_{1,2}$ are the stress and strain induced on each phase, respectively. This model is consistent with the strain partitioning behaviour in dual–phase steels in which ferrite displays lower strength and higher ductility, whereas in martensite most of the external work is due to its higher strength.

In the elastic regime upon yielding, since defining a yield criterion for dual–phase materials is complex [55, 57], the offset yield point at 0.2 % strain is adopted to estimate σ_Y for simplicity. This leads to the macroscopic elastic stress–strain response to be a linear relationship in ε [30]: $\sigma = \sigma_Y(\varepsilon/0.002)$, where the 0.002 factor is the strain offset; ε partitions as $\varepsilon = (1 - V_f)\varepsilon_1 + V_f\varepsilon_2$ [57], where V_f is the martensite volume fraction and ε_1 and ε_2 are the strains on ferrite and martensite, respectively; the previous relation is valid for stress levels up to σ_Y, for $\sigma > \sigma_Y$ a plastic flow rule should be introduced. The elastic stress on each phase is [57]: $\sigma_1 = \sigma_{Ferr}(\varepsilon_1/0.002)$ and $\sigma_2 = \sigma_{Mart}(\varepsilon_2/0.002)$, where σ_{Ferr} and σ_{Mart} are the yield strength of ferrite and martensite, respectively. Combining the previous equations, it can be shown that the yield stress equals [57]:

$$\sigma_Y = 50 + \sum_i (\beta_i^2 x_i)^{1/2} + \frac{V_f\sigma_{Mart}\sqrt{\sigma_{Ferr}} + (1 - V_f)\sigma_{Ferr}\sqrt{\sigma_{Mart}}}{V_f\sqrt{\sigma_{Ferr}} + (1 - V_f)\sqrt{\sigma_{Mart}}}, \tag{9}$$

where the first two terms account for the friction stress and solid solution strengthening (assuming even elemental partitioning) in both phases. It is interesting noting the strain offset of 0.002 (which has been arbitrarily defined) cancels out during the calculations and the macroscopic yield strength only depends on the yield strength on each phase. If no precipitation is occurring in ferrite, σ_{Ferr} is given only by grain boundary strengthening: $\sigma_{Ferr} = \frac{600}{\sqrt{D_{Ferr}}}$, where the Hall–Petch constant has been obtained from [58]. When the

steel is tempered, σ_{Mart} in the previous equation is replaced by $(\sigma_{Mart}^2 + \sigma_p^2)^{1/2}$ to account for carbide precipitation in the martensitic phase.

Equation 9 allows us to estimate the yield strength of dual–phase steels for different initial microstructures for as–quenched conditions and after tempering (equation 6), although two additional considerations are required: *a*) Carbon mostly partitions into martensite, due to its very low solubility in ferrite; the effective carbon concentration in martensite is given by [59] $x_C^{\alpha'} = \frac{x_C}{V_f}(1 - f_p/4)$. *b*) The effective ferrite and prior austenite grains are partitioned by the volume fraction of martensite [60]: $D_{Ferr} = D_g(1 - V_f)^{1/3}$ and $D_{Mart} = D_g V_f^{1/3}$.

5. Results

The model results for the yield stress at room temperature, dislocation density and martensite boundaries are tested against experimental measurements in 7 martensitic and 5 dual–phase steel families. Details on the model implementation and its input parameters are shown in the Appendix. In addition, MATLAB scripts with the model solution for both martensitic and dual–phase steels are included as supplementary material.

Figure 3(a) shows the model predictions and experimental measurements on the yield strength evolution as a function of the tempering temperature in Mart6; the initial microstructure is described in Table 2. The model shows very good agreement for temperatures between 100 and 700 °C; however, it predicts higher values than the experiments for temperatures between 25 and 100 °C. These discrepancies can be due to predicting a higher precipitation strengthening contribution, since carbides might not be fully precipitated at lower temperatures [1], or due to the presence of thin films of retained austenite inducing early work hardening since the carbon content in these steels is higher [29]. Partial precipitation has not been considered in the model, r_p and f_p were considered fixed and their values may not be valid for all tempering conditions; nevertheless, this can be introduced in future work. Figure 3(b) shows the experimental and predicted yield stress evolution for various tempering temperatures of a medium carbon steel (Mart7), and its respective microstructure evolution, (c) the dislocation density and (d) lath width; the

model shows very good agreement with respect to the experiments for all three cases. It is predicted that the strength and microstructure evolution in the steel is practically constant between room temperature and at about 250 °C, since carbon diffusion rate is relatively low and slow carbide precipitation during this stage might occur; these results are in agreement with experimental evidence [1, 4]. At lower temperatures (25–350 °C) the martensite (dislocation density and block boundaries) strengthening contribution is ∼1500 MPa[‡], whereas carbide strengthening accounts for about 300 MPa; solid solution increase the strength by about 190 MPa; martensite contribution gradually decreases upon being only 450 MPa at 700 °C, whereas the relative contribution of the carbides is now ∼540 MPa (assuming the same volume fraction and particle size than at lower temperatures); this shows that the martensite strength gradually decreases with temperature to hold values in the same order of magnitude than those for precipitation hardening. All these results demonstrate that the model is able to completely characterise the martensitic structure and its strength for different processing conditions.

To illustrate the effect of the tempering time in the martensite strength and microstructure evolution, Figure 4 shows the (a) Yield strength, (b) packet, (c) block and (d) lath size evolution in Mart4 tempered at 650 °C; the model again shows very good agreement with most of the measurements. The model predicts a Yield strength ∼1350 MPa in as–quenched conditions, and it gradually decays towards lower values; the experimental packet size shows apparent coarsening, however the block size is almost constant. The lath size coarsens from ∼0.15 μm up to 0.3 μm after two hours. Figure 5(a) shows the effect of block size in the yield strength evolution for the same steel tempered at 650 °C for 75 minutes; the horizonal axis is expressed in terms of $(d_{block})^{-1/2}$ to illustrate the Hall–Petch relationship. Although higher stress levels are predicted due to the lower block size predicted (Fig. 4(c)), the slope in the model is in agreement with the measurements; this result shows that the grain boundary strengthening effect in equation 8 has a weak effect in the overall strength of martensite and most of the strength is due to the very high dislocation density, since this is not affected by the prior–austenite grain

[‡]This value is obtained with the relation: $\sigma^2_{Mart}/\left(\sigma^2_{Mart}+\sigma^2_p\right)^{1/2}$, to account for the relative contribution of each term inside the square–root term; same was done for σ_p.

size. Additionally, temperature effects on the strength and microstructure evolution in Mar4 are shown in Figure 5, (b) the yield strength, (c) and (d) the block and lath size evolution, respectively. The model shows good agreement for temperatures up to 650 °C; however, it overpredicts the yield strength at higher temperatures; these discrepancies can be due to the temperatures being close to the transformation temperature, increasing the boundary coarsening rate [1]. Nevertheless, the lath size coarsening rate shows good agreement with the experiments. These results further support the model's ability to account for tempering effects in the coarsening and yield stress behaviour.

Figure 6(a) shows the yield strength predictions in dual–phase steels employing equation 9 and their comparison against experimental measurements in DP1 with different carbon content, martensite volume fraction and prior–austenite grain size; chemical compositions are displayed in Table 1; each mark represents a different austenite grain size; detailed experimental characterisation can be found in [60]. The model shows remarkable agreement with the experimental measurements, covering wide ranges in composition and initial microstructural conditions. Figure 6(b) shows additional yield stress predictions for DP2, DP4 and DP5 in as–quenched and tempered conditions (Table 1). The model shows very good predictions in the case of DP2 and DP4; however, discrepancies are shown for DP5 (as–quenched), where the model predicts strengths up to 270 MPa higher than the experimental measurements. These discrepancies can be due to the iso–work assumption in equation 9 overestimating the strength for higher martensite volume fraction [57], as the marteniste/ferrite grain morphology and distribution changes with higher martensite fraction [56, 61]; another possibility is the martensitic matrix undergoing static recovery as the intercritical annealing temperatures in DP5 are below the M_s temperature [61]. For the latter, a more sophisticated approach is needed to account for martensite transformation kinetics during the intercritical annealing. Nevertheless, this can be considered in future work. Figure 6(c) shows a comparison between the model predictions and experimental measurements for the yield stress and stress partitioning ratio during various tempering temperatures in DP3; the latter is defined as the ratio between the measured stress in martensite and ferrite and it has been obtained by measuring the nano–hardness

distribution in both phases with micro–indentation [55]. The partitioning ratio in the model is calculated by using the martensite and ferrite strength terms in equation 9, *i.e.* considering iso–work effects: $\frac{\sigma_{Mart}\sqrt{\sigma_{Ferr}}}{\sigma_{Ferr}\sqrt{\sigma_{Mart}}}$. The model shows good agreement with the experimental trends, although it slightly overestimates the yield stress and stress partitioning ratio; this indicates that either the ferrite strength prediction should be higher or the martensite strengthening contribution should be lower.

To illustrate how the martensite volume fraction and carbon content affect the strength evolution in dual–phase steels, Figure 6(d) shows the hypothetical yield strength evolution in a steel with different carbon content and martensite volume fraction, assuming a prior–austenite grain size of 10 μm and no carbides being present for as–quenched conditions. The model predicts strength increments up to 1250 MPa when transitioning form pure ferrite up to fully martensitic steels with 0.5 C wt% content; the carbon content becomes more prominent as the martensite volume fraction increases; these results are in good agreement with early experimental observations for the ultimate tensile strength [59].

6. Discussion

A new modelling framework for describing the microstructure and strength evolution of lath martensite has been proposed. The packet and block size where shown to be proportional to the prior–austenite grain size, where the proportionality constants are determined by the variant number of the austenite/martensite transformation habit planes within an austenite grain and the crystallographic orientation of the laths within a packet, respectively. This result was confirmed with experimental characterisation in several steels. The lath size was obtained by postulating a mechanism where the lath boundary spatial configuration is such that every carbon atom successfully segregates to the lath boundaries; this is controlled by the thickness of the Cottrell atmosphere. The dislocation density evolution was obtained by considering the lattice distortion energy around a lath boundary being equal to the strain energy of the lath dislocation density; the latter was then expressed as a function of the carbon content and the lath size. This assumption is consistent with neutron diffraction measurements on the dislocation density evolution as a

function of the measured lattice strain [3, 25]. Tempering effects were included by considering carbon atoms diffusing away from the lath boundaries and relaxing the Cottrell atmospheres of the boundary dislocations; this leads to lath coarsening by static recovery and was shown to be controlled by the mean atom diffusion length. This mechanism is consistent with Cottrell and Bilby's original model of yielding and strain ageing in ferrite [46]. These results allowed us to describe the yield strength evolution by including substitutional solid solution effects, Hall–Petch strengthening from the block boundaries, carbide precipitation during tempering and lath dislocation hardening. The latter was mostly controlled by the carbon content and tempering conditions. Strength evolution in dual–phase steels was described by employing the iso–work principle, which dictates that the applied work is equal in both phases; this allowed us to obtain an expression for the yield stress which considers the stress and strain partitioning in the equations. These results were successfully applied to several steels covering wide carbon content, prior–austenite grain size, and tempering conditions.

Although the model showed good results with the assumption of Cottrell atmospheres forming at lath boundaries, further work should be done to include the possibility of carbon segregation due to the presence of other phases such as interlath retained austenite or carbides. This would require developing a model for carbon redistribution during quenching to estimate the volume fraction of retained austenite and carbon clustering [18]. Additionally, carbide precipitation kinetics was not considered and the volume fraction and mean radius were mostly obtained from experiments. Future work will be on introducing a model for precipitation kinetics, since it is well established that a higher boundary and dislocation density promotes carbide precipitation [62]. These features will allow us to modify the assumption that not all carbon atoms segregate towards the lath boundaries in the form of Cottrell atmospheres and introduce cooling rate and M_s effects. Additional extensions to this work include considering compositional effects on carbon diffusion and the martensitic structure other than pure carbon and solid solution strengthening; higher carbon steels will require revisiting the crystallographic features of the transformation mechanism, introducing lattice strain accommodation by twinning

within the martensite plates and carbon partitioning into the retained austenite; this can be done in future work. Additionally, dislocation evolution during strain hardening can be further described to obtain the ultimate–tensile strength and elongation evolution with different heat treatments.

6.1 Tempering effects on martensite strength

One of the most important parameters for alloy design in martensite–containing steels is the tempering step, since the material's ductility and toughness can increase with respect to the as–quenched material, although the tensile strength can be drastically reduced without a proper tempering schedule [4]. To the authors knowledge, only qualitative insights for tempering design are available and these are mostly based on empirical evidence. The aim of this work is to provide a mathematical tool that can quantitatively describe the strength contribution of the martensitic structure under different processing routes and chemical compositions. For instance, Figure 7 shows a parametric analysis on the martensite stress (σ_{Mart}) evolution under different tempering temperatures and times in a (a) low (0.25 wt%) and (b) medium (0.5 wt%) carbon steel (only Fe and C are considered); an austenite grain size was assumed equal to 20 μm and carbide strengthening was neglected for simplicity. It is worth noting that precipitation hardening contributions should be properly accounted for to prescribe the actual yield stress values. The contour lines represent the conditions for constant stress; these lines increase in steps of 50 MPa in (a), and in steps of 100 MPa in the remaining figures. In the case of the lower carbon steel, the model predicts a constant martensite strength contribution of 1050 MPa if the steel is tempered at 475 °C for 0.25 hours than if it were tempered at 300 °C for nearly 3 hours. A similar case occurs for the medium carbon steel. Moreover, Figure 7(c) and (d) respectively show the temperature and time effects of tempering for steels with different carbon content; same initial conditions were assumed than in the previous case. The model predicts (Fig 7(c)) that the same martensite strength contribution of 1000 MPa can be obtained in a low carbon steel with 0.21 C (wt%) tempered at temperatures below 300 °C and than in a medium carbon steel (C$\geq$ 0.3 wt%) tempered at temperatures in

excess of 450 °C. Tempering time effects are less sensitive to strength evolution, although higher precipitation strengthening contribution might be present [24]. These results illustrate that poorly–designed tempering treatments may lead to overaging conditions where the yield strength may dramatically decrease.

7. Conclusions

The following conclusions can be outlined from this work:

- A new model for the microstructure and strength evolution of lath martensite has been introduced. This includes predicting the packet, block and lath size, the dislocation density and yield stress for various compositions and tempering conditions.

- A mechanism for the lath boundary arrangement has been proposed. This is based upon considering the lath boundary spacing to be arranged in such form that it ensures complete carbon segregation to the lath boundaries after the transformation occurs. It was found that the lath size is controlled by the thickness of Cottrell atmospheres and the carbon concentration available for segregation.

- The dislocation density was shown to be proportional to the lattice strain by carbon atoms and it is inversely proportional to the lath size. The former is related to the shear strains from the supersaturated carbon content in the matrix during the phase transformation.

- Tempering effects were introduced by estimating the carbon fraction diffusing away from the Cottrell atmospheres of the lath–boundary dislocations; this mechanism simultaneously induces dislocation recovery and lath boundary coarsening.

- The yield stress of martensite can be predicted by only introducing a block boundary strengthening, dislocation density and carbide strengthening terms; the latter becomes active during tempering. It was also shown in 0.56 C wt% (Mart7) that at lower tempering temperatures most of the martensite's strength is dictated by

dislocations and this gradually decreases upon being about the same value than carbide strengthening.

- By using the iso–work principle, it was shown that the predicted stress partitioning ratio in ferrite and martensite and yield stress were very close to the experimentally–measured values in dual–phase steels.

Acknowledgements

This research was supported by the grant EP/L025213/1 from the UK Engineering and Physical Sciences Research Council (EPSRC).

Appendix

The main equations of the yield stress model for martensitic steels are the strength of martensite (8), lath dislocation density (5), lath thickness (in as-quenched 3 and tempered 6 conditions), carbon partitioning in the matrix, block size (2) and precipitation strengthening (7):

$$\begin{aligned}
\sigma_Y &= 50 + \sum_i (\beta_i^2 x_i)^{1/2} + \left(\sigma_{Mart}^2 + \sigma_p^2\right)^{1/2} \\
\sigma_{Mart} &= \frac{300}{\sqrt{d_{block}}} + 0.25 M \mu b \sqrt{\rho}, \\
\rho &= \frac{3E}{(1+2\nu^2)\mu} \frac{4\varepsilon^2 d_{Cottrell}}{d_{lath}^2 b} \\
x_C^{\alpha'} &= x_C(1 - f_p/4) \\
d_{lath} &= d_{lath,0} + \lambda_0 x_C^{\alpha'} \sqrt{D_{diff} t} \\
d_{lath,0} &= d_{Cottrell} (x_C^{\alpha'})^{2/3} \\
d_{block} &= 0.067 D_g \\
\sigma_p &= 0.26 \frac{\mu b}{r_p} f_p^{1/2} \ln\left(\frac{r_p}{b}\right).
\end{aligned} \tag{10}$$

The model parameters for σ_{Mart} and ρ are: $M = 3$ [52]; $d_{Cottrell} = 7$ nm is taken from atom–probe measurements [14]; λ_0 is a fitting constant accounting for a diffusion barrier for carbon atoms segregated into Cottrell atmospheres, and it is adjusted as $b/d_{Cottrell}$ to validate the yield stress model with experimental data of the tested steels. The input parameters for the precipitation hardening term (f_p and r_p) are listed in Table 2 in Section 2.

The solid solution constants β_i are estimated with Fleischer's formula [23, 49]: $\beta_i = \kappa\mu(\eta_i' + 16\delta_i)^{3/2}$, where κ is a fitting parameter; $\eta_i' = \eta_i/(1 + 0.5\eta_i)$ is a constant; $\eta_i = \frac{|\mu_i - \mu_{Fe}|}{\mu_{Fe}}$ and $\delta_i = \frac{|r_i - r_{Fe}|}{r_{Fe}}$ are the modulus and lattice distortion of element i with respect to pure iron, respectively; and μ_i and r_i are the shear modulus and atomic radius of element i obtained from [63], respectively. $\kappa = 0.0045$ was obtained by adjusting β_i to the measured critical–resolved shear stress of Fe–based alloys obtained from [64]. Table 3 shows the values of these parameters for the alloying elements employed in this work.

The main equations of the yield stress model for dual–phase steels are the strength of the respective phase (8), carbon partitioning into the martensite and grain sizes:

$$\begin{aligned}
\sigma_Y &= 50 + \sum_i (\beta_i^2 x_i)^{1/2} + \frac{V_f \sigma_{Mart}\sqrt{\sigma_{Ferr}} + (1 - V_f)\sigma_{Ferr}\sqrt{\sigma_{Mart}}}{V_f\sqrt{\sigma_{Ferr}} + (1 - V_f)\sqrt{\sigma_{Mart}}}, \\
\sigma_{Ferr} &= \frac{600}{\sqrt{D_{Ferr}}}, \\
x_C^{\alpha'} &= \frac{x_C}{V_f}(1 - f_p/4), \\
D_{Ferr} &= D_g(1 - V_f)^{1/3}, \\
D_{Mart} &= D_g V_f^{1/3}
\end{aligned} \tag{11}$$

In this case, $x_C^{\alpha'}$ and D_{Mart} are used to estimate d_{lath}, d_{block} and σ_{Mart}. The remaining parameters for martensite are those employed in pure martensitic steels.

References

[1] Bhadeshia HKDH, Honeycombe RWK. *Steels: Microstructure and properties.* Butterworth-Heinemann 2006.

[2] Morito S, Nishikawa J, Maki T. *ISIJ* 2003;43:1475.

[3] Christien F, Telling MTF, Knight KS. *Scripta Mater* 2013;68:506.

[4] Krauss G. *Steels: Processing, structure and performance.* ASM international 2005.

[5] Morito S, Adachi Y, Ohba T. *Mater Trans* 2009;50:1919.

[6] Furuhara T, Kawata H, Morito S, Maki T. *Mater Sci Eng A* 2006;431:228.

[7] Zhang S, Morito S, Komizo , Y . *ISJ* 2012;52:510.

[8] Kitahara H, Ueji R, Tsuji N, Minamino Y. *Acta Mater* 2006;54:1279.

[9] Morito S, Yoshida H, Maki T, Huang X. *Mater Sci Eng A* 2006;438:237.

[10] Zhang C, Wang Q, Ren J, et al. *Mater Sci Eng A* 2012;534:339.

[11] Zhang C, Wang Q, Ren J, et al. *Mater Design* 2012;36:220.

[12] Hoseiny H, Caballero FG, San Martin D, Capdevilla C. *Mater Sci Forum* 2012;706:2140.

[13] Miller MK, Beaven PA, Brenner SS, Smith GDW. *Metall Trans A* 1983;14:1021.

[14] Wilde J, Cerezo A, Smith GDW. *Scripta Mater* 2000;43:39.

[15] Hutchinson B, Hagström J, Karlsson O, et al. *Acta Mater* 2011;59:5845.

[16] Chang L, Banard SJ, Smith GDW. ' *Proc 30th Int Field Emission Symposium* 1983:19.

[17] Smith GDW, Hudson D, Styman PD, Williams CA. *Phil Mag* 2013;93:28.

[18] Sherman DH, Cross SM, Kim S, Grandjean F, Long GJ, Miller MK. *Metall Mater Trans A* 2007;38:1698.

[19] Chen P, Ghassemi-Armaki H, Kumar S, Bower A, Bhat S, Sadagopan S. *Acta Mater* 2014;65:133.

[20] Hou Z, Hedström P, Xu Y, Di W, Odqvist J. *ISIJ Int* 2014;54:2649.

[21] Wu Q, Zikry MA. *Int J Solids Struct* 2014;51:4345.

[22] Rivera-Díaz-del-Castillo PEJ, Hayashi K, Galindo-Nava EI. *Mater Sci Tech* 2013;29:1206.

[23] Fleischer RL. *Acta Metall* 1963;11:203.

[24] Baltazar Hernandez VH, Nayak SS, Zhou Y. *Metall Mater Trans A* 2011;42:3115.

[25] Kim B, Boucard E, Sourmail T, San Martín D, Grey N, Rivera-Díaz-del-Castillo PEJ. *Acta Mater* 2014;68:169.

[26] Villa M, Pantleon K, Reich M, Kessler O, Somers MAJ. *Acta Mater* 2014;80:468.

[27] Sarikaya M, Jhingan AK, Thomas G. *Metall Trans A* 1983;14:1121.

[28] Sandvik BPJ, Wayman CM. *Metallography* 1983;16:199.

[29] Morito S, Oh-Ishi K, Hono K, Ohba T. *ISIJ* 2011;51:1200.

[30] Dieter G E. *Mechanical Metallurgy*. McGraw Hill 1988.

[31] Morito S, Tanaka H, Konishi R, Furuhara T, Maki T. *Acta Mataer* 2003;51:1789.

[32] Kinney CC, Pytlewski KR, Khachaturyan AG, Morris Jr. JW. *Acta Mater* 2014;69:372.

[33] Morito S, Saito H, Ogawa T, Furuhara T, Maki T. *ISIJ* 2005;45:91.

[34] Oslon GB, Cohen M. *Metall Trans A* 1976;7:1897.

[35] Sherby OD, Wadsworth J, Lesuer DR, Syn CK. *Mater Trans* 2008;49:2016.

[36] Iwashita K, Murata Y, Tsukada Y, Koyama T. *Phil Mag* 2011;91:4495.

[37] Hull D, Bacon DJ. *Introduction to dislocations*. Butterworth-Heinemann 1999.

[38] Clarke AJ, Miller MK, Field RD, et al. *Acta Mater* 2014;77:17.

[39] Apple CA, Caron RN, Krauss G. *Metall Trans* 1974;5:593.

[40] Swarr T, Krauss G. *Metall Trans A* 1976;7:41.

[41] Ghassemi-Armaki H, Chen RP, Maruyama K, Yoshizawa M, Igarashi M. *Mater Letters* 2009;63:2423.

[42] Stibitz GR. *Phys Rev* 1936;49:859.

[43] Xiao L, Fan Z, Jinxiu Z. *Phys Rev B* 1995;52:9970.

[44] Udyansky A, von Pezold J, Bugaev VN, Friák M, Neugebauer J. *Phys Rev B* 2009;79:224112.

[45] Caron RN, Krauss G. *Metall Trans* 1972;3:2381.

[46] Cottrell AH, Bilby BA. *Proc Phys Soc A* 1949;62:49.

[47] Argon A S. *Strengthening mechanisms in crystal plasticity*. Oxford University Press 2008.

[48] Gladman T. *Mater Sci Tech* 1999;15:30.

[49] Toda-Caraballo I, Galindo-Nava EI, Rivera-Díaz-del-Castillo PEJ. *Acta Mater* 2014;75:287.

[50] Daigne J, Guttman M, Naylor JP. *Mater Sci Eng* 1982;56:1.

[51] Shibata A, Nagoshi T, Sone M, Morito S, Higo Y. *Mater Sci Eng A* 2010;527:7538.

[52] Kocks UF, Mecking H. *Prog Mater Sci* 2003;48:171.

[53] Queyreau S, Monnet G, Devincre B. *Acta Mater* 2010;58:5586.

[54] Jiang Z, Guan Z, Lian J. *Mater Sci Eng A* 1995;190:55.

[55] Han Q, Asgari A, Hodgson PD, Stanford N. *Mater Sci Eng A* 2014;611:90.

[56] Tasan CC, Hoefnagels JPM, Diehl M, Yan D, Roters F, Raabe D. *Int J Plast* 2014;63:198.

[57] Bouaziz O, Buessler P. *Adv Eng Mater* 2003;6:79.

[58] Takaki S. *Mater Sci Forum* 2010;654:11.

[59] Chen HC, Cheng GH. *J Mater Sci* 1989;24:1991.

[60] Chang PH, Preban AG. *Acta Metall* 1985;33:897.

[61] Chakraborti PC, Mitra MK. *Mater Sci Eng A* 2007;466:123.

[62] Kozeschnik E. *Modeling solid-state precipitation*. Momentum press 2013.

[63] Lide DR. *CRC Handbook of Chemistry and Physics*. CRC Press 2008.

[64] DePaul RA, Kitchin AL. *Metall Trans* 1970;1:389.

[65] Yan P, Liu Z, Bao H, Weng Y, Liu W. *Mater Sci Eng A* 2014;597:148.

[66] Wang Q, Zhang C, Li R, Gao J, Wang M, Zhang F. *Mater Sci Eng A* 2013;559:130.

[67] Saeglitz M, Krauss G. *Metall Mater Trans A* 1997;28:377.

[68] Hasegawa K, Toji Y, Minami H, Ikeda H, Morikawa T, Higashida K. *Testu-to-Hagané* 2012;98:106.

[69] Sudersanan PD, Kori N, S Aprameyam, Kempaiah UN. *Bonfring Int J Ind Eng Man Sci* 2012;2:1.

Table 1: Chemical composition (in wt%) of the steels tested in this work.

Steel	C	Si	Mn	Cr	Al	Ni	Mo	Co	W	Ref.
Mart1	0.076	-	-	8.83	-	-	–	2.99	3.11	[65]
Mart2	0.12–0.48	0.23–1.25	0.77–1.7	0–1.31	0.04–0.13	0–0.81	-	-	-	[15]
Mart3	0.2	0.01	0–2	-	-	-	-	-	-	[9]
Mart4	0.25	0.26	0.5	1	0.03	0.04	0.75	-	-	[10, 11, 66]
Mart5	0.39	0.27	1.36	1.95	-	1	-	-	-	[12]
Mart6	0.4	0.27	0.69	0.79	0.03	1.78	0.26	-	-	[67]
Mart7	0.56	1.4-2.3	0.69-0.72	0.89	-	-	-	-	-	[25]
DP1	0.034–0.23	0.01	0.22-0.35	-	-	-	-	-	-	[60]
DP2	0.05–0.18	1.47	2	-	-	-	-	-	-	[68]
DP3	0.1	0.92	2	0.03	0.03	-	-	-	-	[55]
DP4	0.13	0.3	1.18	0.047	-	-	-	-	-	[69]
DP5	0.21	0.1	1.7	-	-	-	-	-	-	[61]

Table 2: Heat–treatment conditions and initial microstructures of the studied steels.

Steel	Conditions	t (min)	T (°C)	D_g (μm)	r_p (nm)	f_p (%)	V_f (%)	Ref.
Mart1	Tempered	60	260	20–70	-	-	-	[65]
Mart2	As–quenched	-	-	10–40	-	-	-	[15]
Mart3	As–quenched	-	-	5–400	-	-	-	[9]
Mart4	Tempered	0–75	600–700	10	25	11	-	[10, 11, 66]
Mart5	Tempered	240	540	20–80	-	-	-	[12]
Mart6	Tempered	60	25–650	20	25	8	-	[67]
Mart7	Tempered	30	250–450	12	7.5	8	-	[25]
DP1	Tempered	10	260	7–93	50	10	3–51	[60]
DP2	Tempered	30	150	12	50	10	25–72	[68]
DP3	Tempered	10	280–550	9.8	50	10	54	[55]
DP4	As–quenched	-	-	20	-	-	47–69	[69]
DP5	As–quenched	-	-	25	-	-	38–80	[61]

Table 3: Solid solution constants.

Element	r_i (nm)	μ_i (GPa)	δ_i (nm/nm)	η_i (GPa/GPa)	β_i (MPa/at)
Fe	0.124	80	-	-	-
Al	0.124	26	0	0.67	129
Cr	0.130	115	0.05	0.43	434
Mn	0.129	75	0.04	0.06	213
Mo	0.146	126	0.17	0.57	2143
Ni	0.117	76	0.06	0.05	334
Si	0.114	50	0.08	0.37	732

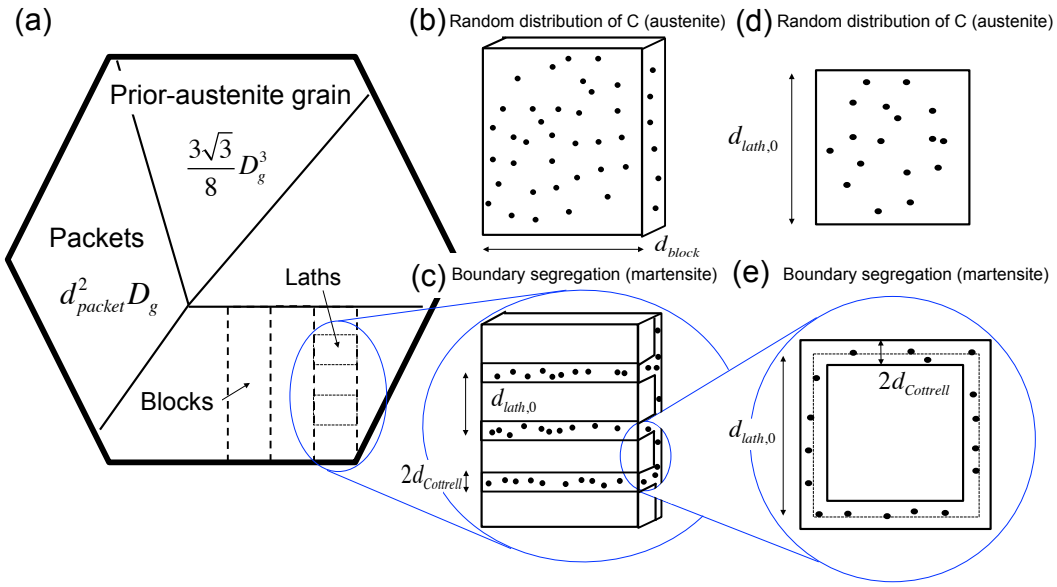

Figure 1: (a) Schematic illustration of a martensite hierarchical structure within a prior–austenite grain size. (b–e) Comparison between the cross–sectional area covered by carbon in austenite (random distribution) and in martensite (high segregation into the lath boundaries). (b) and (c) show the comparison at the block level, whereas (d) and (e) show carbon distribution at the lath–boundary level.

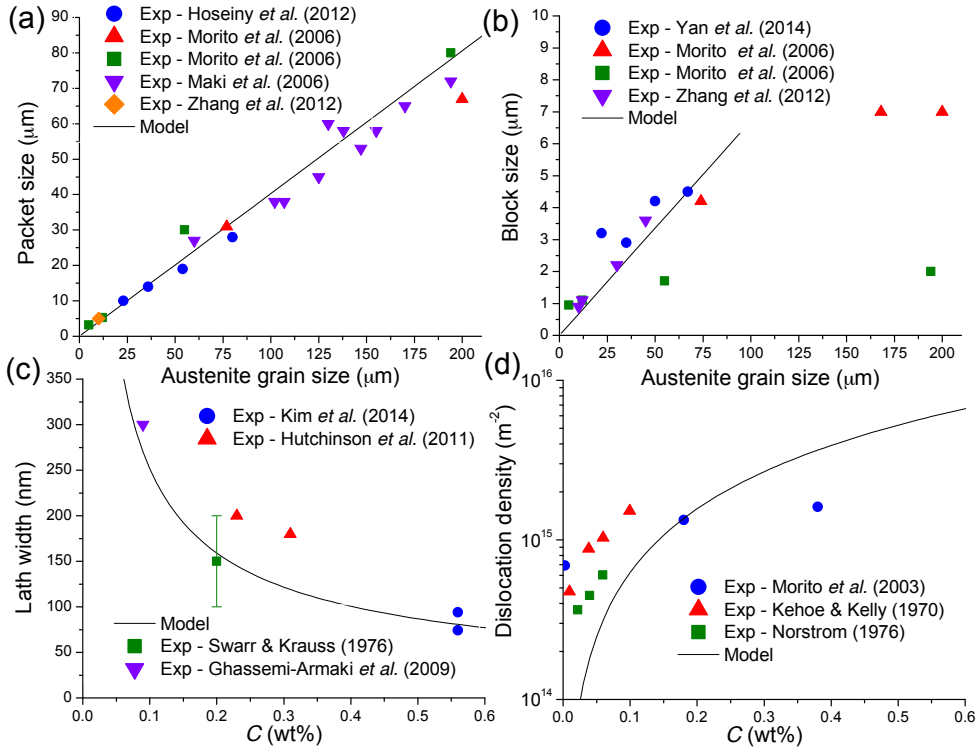

Figure 2: Link between the prior–austenite grain size and (a) packet and (b) block size in various steels. (c) Lath width and (d) dislocation density variation as a function of the carbon content in martensite.

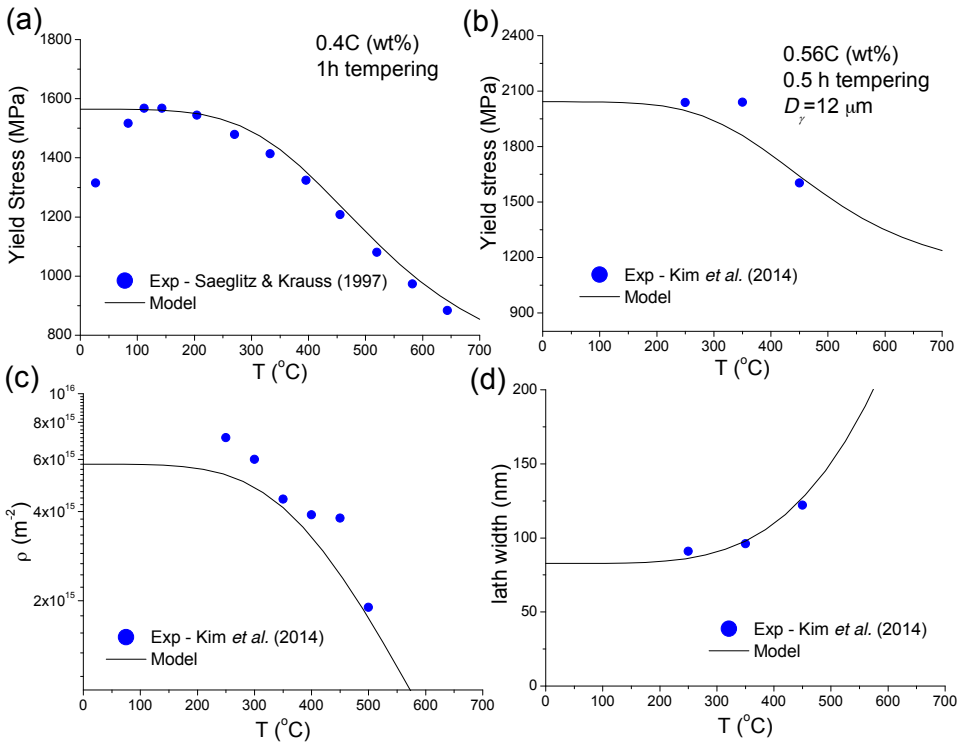

Figure 3: (a) Yield stress predictions for different temperatures in Mart6. (b) Yield stress, (c) dislocation density and (d) lath width predictions and comparison with experiments in Mart7.

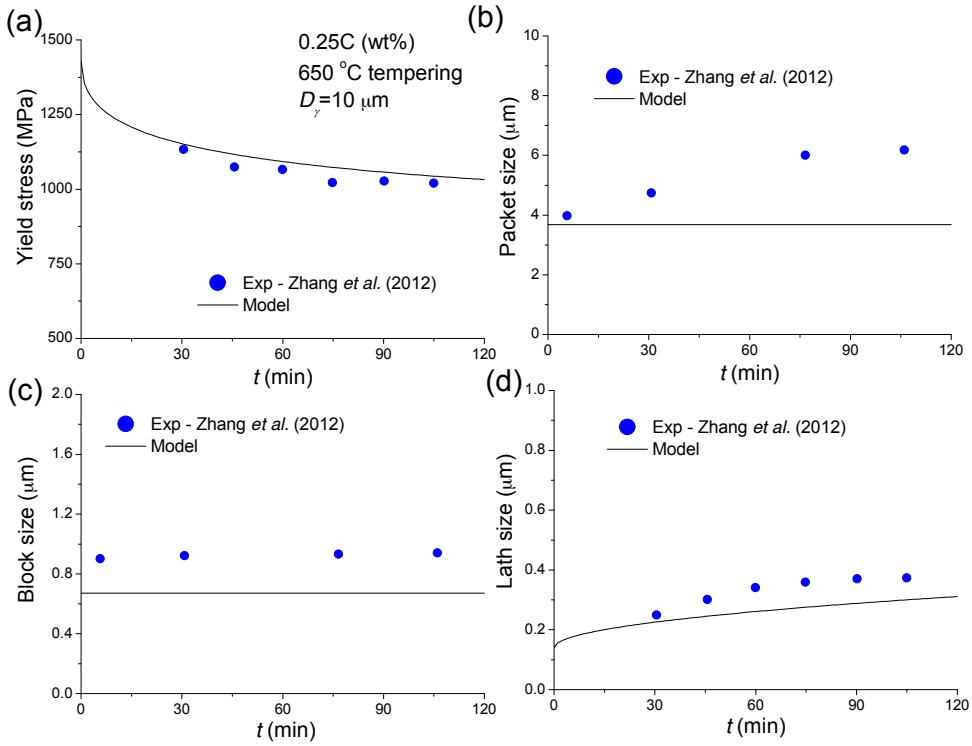

Figure 4: Effect of the tempering time in Mart4 and the evolution of (a) Yield stress, (b) packet, (c) block, and (d) lath size.

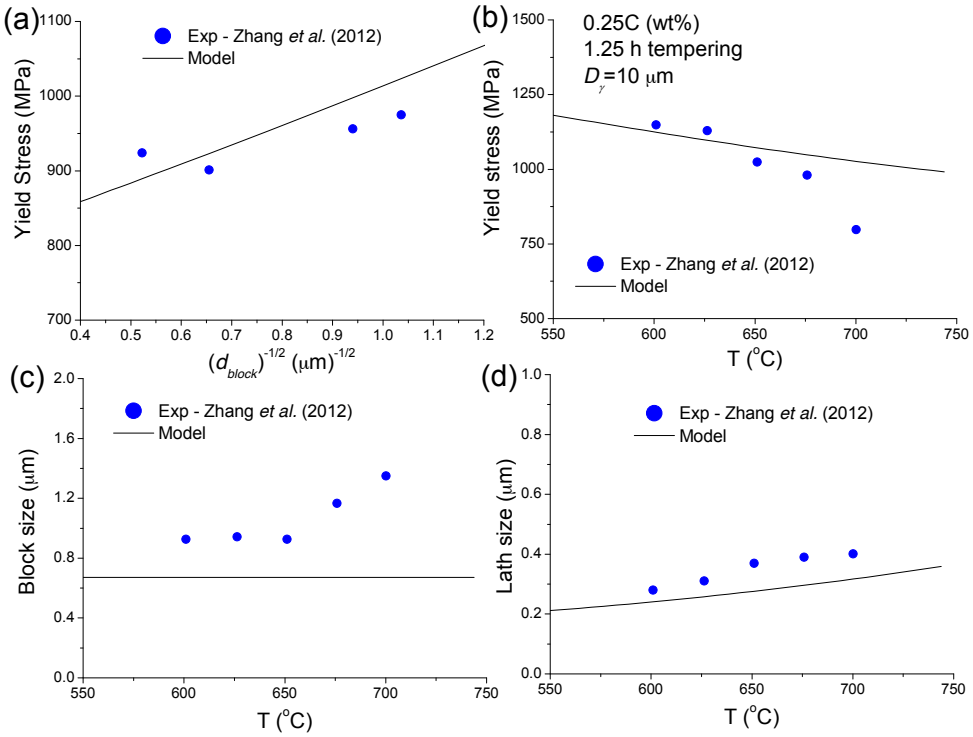

Figure 5: (a) Block size effects on the yield strength in Mart4. Effects of the tempering temperature in Mart4 and the evolution of (b) Yield stress, (c) block, and (d) lath size.

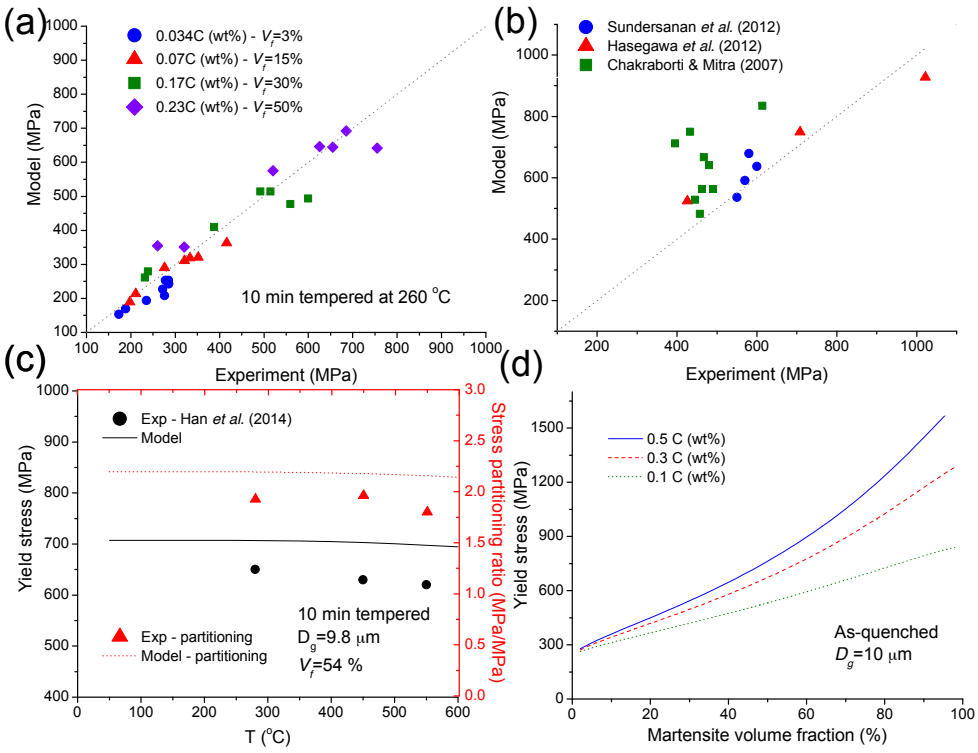

Figure 6: (a) Comparison between yield stress predictions and experiments in DP1 for various austenite grain sizes and martensite volume fractions; (b) additional predictions in DP2, DP4 and DP5. (c) Yield stress and stress partitioning predictions in DP3. (d) Carbon content and martensite volume fraction effects in the yield stress evolution.

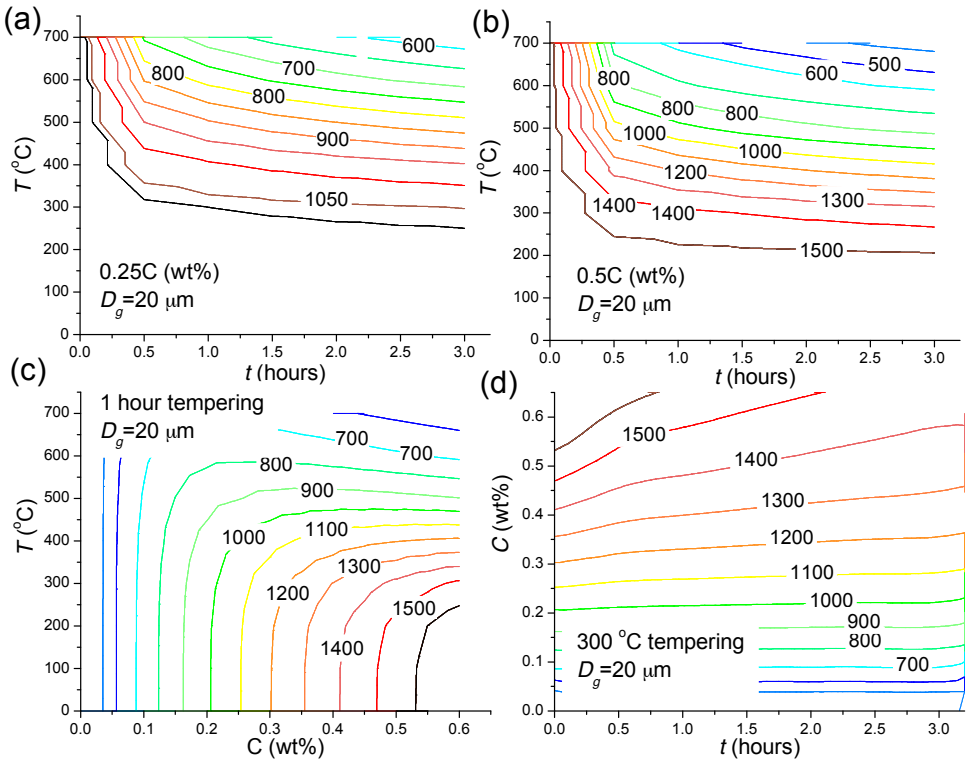

Figure 7: Parametric analysis on tempering conditions affecting the martensite strength for (a) Fe–0.25C (wt%) and (b) Fe–0.5C (wt%). Carbon effects on the tempering (c) temperature and (d) time. The contour lines delineate iso–stress.